Energies **2013**, *6*, 3841-3858; doi:10.3390/en6083841

OPEN ACCESS

energies

ISSN 1996-1073

www.mdpi.com/journal/energies

Article

Results of Current Density Distribution Mapping in PEM Fuel Cells Dependent on Operation Parameters

Maik Heuer *, Paul A. Bernstein, Michael Wenske and Zbigniew A. Styczynski

Otto-von-Guericke University Magdeburg, Chair Electric Power Networks and Renewable Energy Sources, Universitätsplatz 2, D-39106 Magdeburg, Germany; E-Mails: paul.bernstein@ovgu.de (P.A.B.); michael.wenske@ovgu.de (M.W.); sty@ovgu.de (Z.A.S.)

* Author to whom correspondence should be addressed; E-Mail: maik.heuer@ovgu.de; Tel.: +49-391-67-18296; Fax: +49-391-67-12408.

Received: 13 June 2013; in revised form: 15 July 2013 / Accepted: 19 July 2013 / Published: 29 July 2013

Abstract: This paper presents *in situ* measurements of a newly developed current density measurement system for proton exchange membrane fuel cells (PEMFC). While the functional principle and technical evaluation of the measurement system were presented in a previous paper, this paper analyzes the influence of various operation parameters, including multiple start-stop operation, at the anode, cathode and cooling locations on the distribution and long-term development of the current density. The system was operated for 500 h over two years with long periods of inactivity between measurements. The measurement results are evaluated and provide additional information on how to optimize the operation modes of fuel cells, including the start and stop of such systems as well as the water balance.

Keywords: PEM fuel cell; current density measurement; current density distribution; operation optimization

---

1. Introduction

The operation conditions and the required sensor and actuator technology have an important influence on costs, power and energy density, efficiency, long-term behavior and integration options for PEM fuel cell (PEMFC) systems. Basic studies [1–5] help to optimize stack and system development. Some methods to analyze the system behavior online go even further. Insights gained

during the operation of the PEMFC can not only change the system design but also the optimization of the operation conditions itself and subsequently can be used for system control. Even though recent activities in approved methods to analyze the system behavior during operation (e.g., electrochemical impedance spectroscopy [6,7] or neutron radiography for investigation of water accumulation [8,9]) show further improvements, they still require adapted cell configurations and more or less extensive measurement arrangements or can even damage the cell permanently. The current density distribution measurement (CDM) makes it possible to obtain deeper insight during operation.

This paper uses a measurement system design for CDM, without major impacts on cell configuration or costs and ready to be used as an instrument for operational measurements. The technical demands like resolution, sample time and the measurement principle were discussed in detail in [10]. The new hardware CDM system was field-tested for two years with various starts and stops, offline periods, varied operation parameters and a deep analysis of the current density profile, the cell voltages, the humidity balance and general performance and degradation. The results from the measurements are presented and discussed in detail in the paper.

2. Measurement and Experimental Setup

For the research, a specified test stand built by the German company Inhouse Engineering (Berlin, Germany) was used. It is composed of a four-cell PEM fuel cell stack from the same company with an active MEA area of 196 cm^2. The current density *j* defines the current flow through a defined conductor cross-section. The fuel cell current I_{FC} is related to the active cell area A_{Cell} and is used as a reference value for comparison of the fuel cell while A_{Seg} is the area of one segment [Equation (1)]:

$$j = \frac{I_{FC}}{A_{Cell}} = \frac{\sum_i^n I_i}{n \cdot A_{Seg}} \quad (1)$$

A CDM board is integrated between the two central cells [10], which maps the distribution of the electricity production over the active area. The characteristics of the CDM are presented in Table 1. The sensor unit is arranged on a printed circuit board (PCB in Figure 1) consisting of a shunt matrix with 112 elements to determine the local current densities. The shunt resistors have a low temperature coefficient (below 0.13% between 20 and 80 °C), are low ohmic (with a resistor value tolerance of 1%), and are embedded in a solid epoxy resin layer and connected by buried vias to the 112 segments which are in contact with the adjacent bipolar- and cooling plates [10]. A high resolution 15 bit ΣΔ-Analogue-Digital-Converter ensures the accuracy of the digitization with a sufficient sampling time of 4 Hz. Furthermore each segment is calibrated with a calibration tool with an accuracy of 0.2% for the measured currents [10].

Additionally the LENA Pro (a self-developed differential single cell voltage measurement system using anoalog-to-digital converters with a high resolution) [11] measures the voltage of each individual cell. The nominal operating point of the stack is 100 A which results in a power output of 260 W. The supplied industrial grade hydrogen 5.0 from Linde and the filtered air flow in the same direction (co-flow) through the channels of the graphite bipolar plates, which are arranged horizontally.

Figure 1. (**a**) Schematics of the CDM and (**b**) PEMFC stack with 4 cells and integrated 112 segments PCB for the CDM.

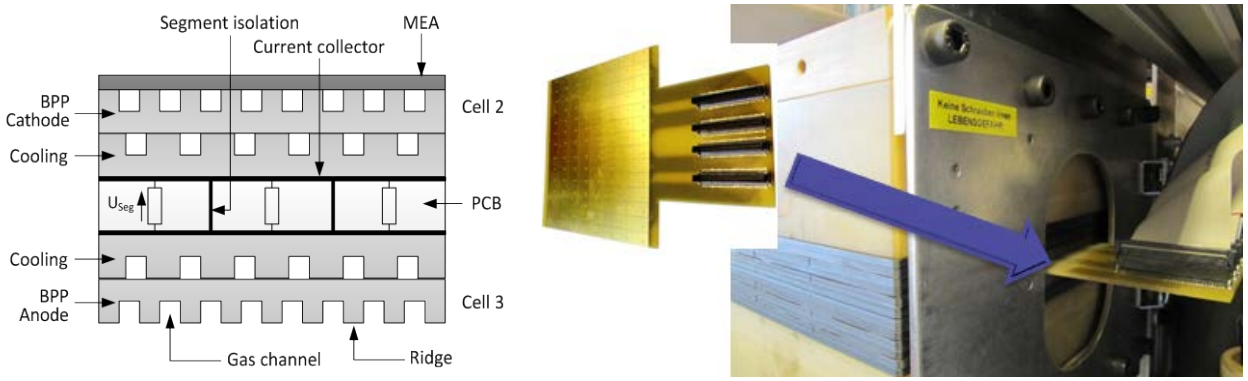

(**a**) (**b**)

The anodic channel geometry is designed for operation with hydrogen and active recirculation. The cathode operates in overflow mode, which means the unused exhaust air is released into the atmosphere without further usage for prehumidification or heating. Both the anodic and cathodic loops are purged with nitrogen before and after operation to convey condensate, foreign gases and solid particles from the fuel cell and pipe system.

Table 1. Characteristics of the CDM.

Element	Characteristic	Value
Sensor layer	Printed circuit board (PCB)	Multilayer PCB with two-way segmentation
	Measuring segments	112 (8 × 14)
	Resistors	1% tolerance, R = 150 mΩ
	Long-term stability of the resistors	0.5%/2000 h (70 °C)
	Area per segment	A_{Seg} = 1.74 cm^2 (A_{PCB} = 194.88 cm^2)
	Area loss due to insulation	2.8% (200 µm)
	Current load per segment	0–1.1 A
	Power loss per measurement resistor	119.6 mW@100 A (13.4 W for full PCB)
	Contact resistance to the Bipolar Plate (BPP)	3.34–6.25 mΩ per side(calculated)
Electronics	Microprocessor	ATmega
	Resolution	15 bit
	Interface	RS-232 or USB via adapter
	Fuel cell current	0–120 A
	Deviation of the voltage measurement	<0.07% over the whole measuring range
	Conversion time of one data block	<250 ms
Evaluation	Program	NI LabVIEW or MathWorks MATLAB
	Storage interval	from 0.5 s
	Storage format	txt or csv

Figure 2 shows the system diagram of the tested system. The filtered air is humidified to 90%–100% rH (controlled with a HUMICAP® HMT 330 by Vaisala, Vantaa, Finland) and heated to the set point temperature by a bubbler. The dry hydrogen tube leads through a thermostat basin for preheating and is mixed with the moist recycled hydrogen before entering the fuel cell. Condensed water is removed

through steam traps. A purge valve is positioned at the output of the anodic loop, which opens at defined intervals for one s to remove inert gas and condensate enrichments. Additional operating conditions are listed in Table 2, however some conditions were modified during measurements to see the impact on the current density (see Section 4).

Figure 2. Schematics of the PEMFC System.

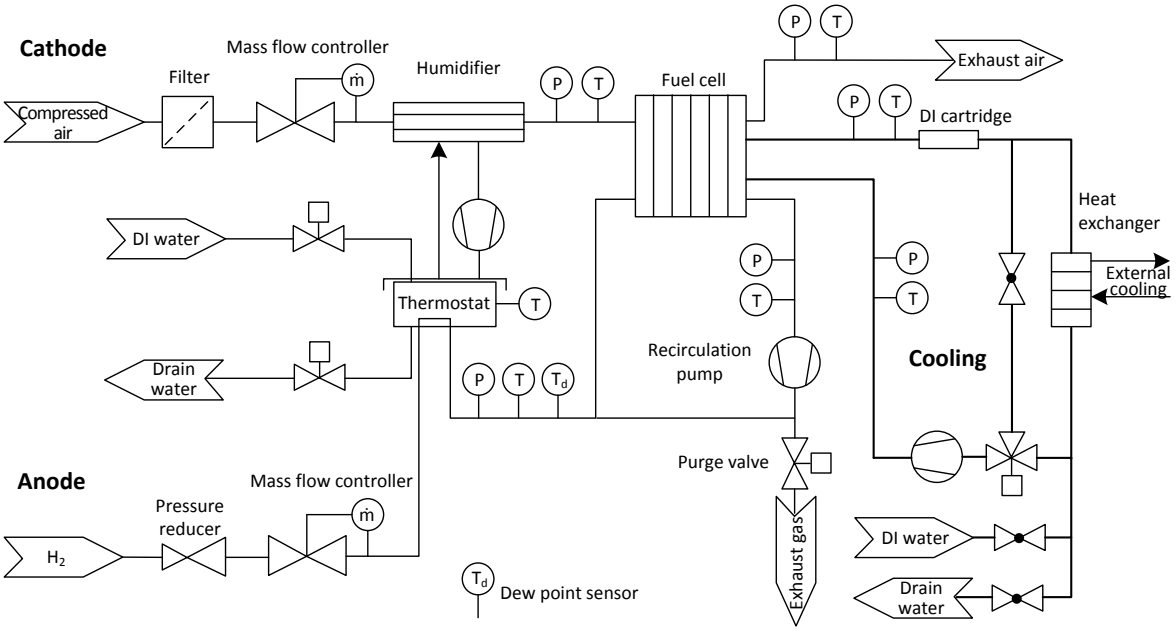

Table 2. Characteristics of the PEMFC for stationary application.

Element	Characteristic	Value
Stack	Number of cells	$n_{FC} = 4$
	Active cell area	$A_{cell} \approx 196$ cm^2
	Bipolar flow direction	coflow, internal manifold
	Alignment of the bipolar plates	horizontal
Electronics	Fuel cell voltage	$U_{FC} = 2.64$ V (single-cell voltage measurement)
	Rated current	$I_{FC,rated} = 100$ A
	Rated electrical power	$P_{FC,el} = 260$ W@100 A (≈ 500 mA/cm^2)
	minimal single cell voltage	$U_{cell,min} = 500$ mV
Anode side	Operating mode	Active recirculation with purge valve
	Humidification	Self-humidification by recirculation
	Anode inlet pressure	$p_{An,in} \approx 230$ mbar@(2.78 Nl/min+recirculation)
Cathode side	Operating mode	Overflow
	Humidification	$\varphi \approx 0.9$–1; Water-gas-membrane-humidifier
	Cathode inlet pressure	$p_{Ca,in} = 120$ mbar@16.7 Nl/min
	Stoichiometry	$\lambda_{An} \approx 2.5$–3.0
	Air quality (particle size)	≤ 5 µm
Cooling circuit	Operating temperature	$T_{FC} = 50$–80 °C (outlet temperature of DI water)
	Conductivity of DI water	$\sigma_{H2O} = \leq 5$ (µS/cm)

3. Experimental Procedure

3.1. Measuring Process and Conditions

All measurements were performed according to the load profile in Figure 3. At the beginning of the measurement, the current density is increased at two min intervals, by 100 mA/cm^2 up to the nominal operating point of 500 mA/cm^2. For each measurement the same starting parameters were used in the constant phase (see Figure 3, measurement time 0–5 h). After 5 h, the parameters were varied to determine the dependence of operating parameters of the polarization curve and the current density (variation phase).

Figure 3. Load profile with constant parameter and parameter variation phase.

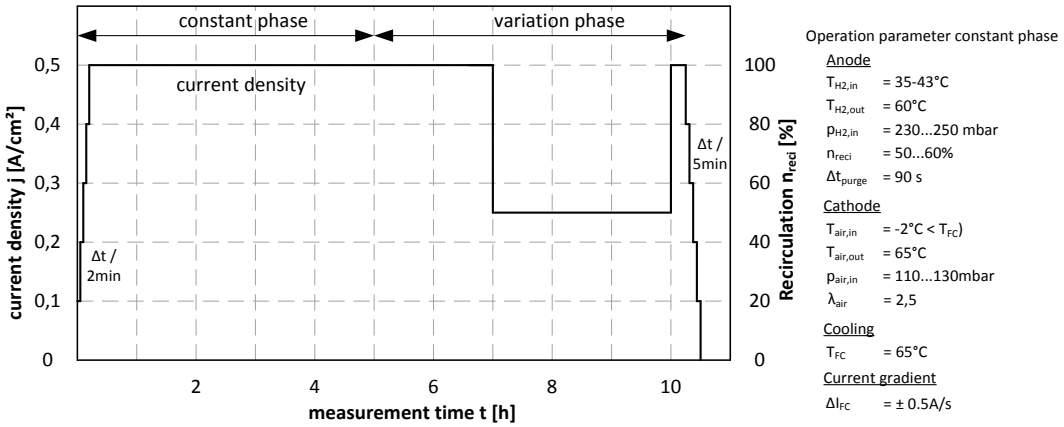

The measurements and the ranges in which the parameters were varied are summarized in Table 3. The measurements with a measurement time of 11 h were repeated at least once for unambiguous determination of the current density behavior. After the reference measurement (measurement 1) of 100 h, the rotational speed of the recirculation pump was varied between 50% and 100% and the interval between purging successively increased up to 11 min. The stoichiometry at the cathode was varied between 2 and 4 and the inlet air temperature was varied between 59 and 65 °C. The impact of the increase of stack temperature from 65 to 70 °C was analyzed in measurements 13 and 14. After another 100 h measurement period the direction of flow of the gases was reversed to analyze the impact on the current density profile (measurement 18).

Table 3. Measurement overview of the investigated parameter related to the CDM.

Measurement (MR#)	Title	Parameter variation	Measurement time	Value range
1	Reference	-	100 h	-
2,3	Recirculation	n_{Reci}	11 h	50%–100%
4,5	Purge interval	Δt_{Purge}	11 h	30–660 s
6,7	Stoichiometry	λ_{air}	11 h	2–4
8,9,10	Temp. air inlet	$T_{air,in}$	11 h	59–65 °C
11,12	Stoichiometry	λ_{air}	11 h	2.2–2.5
13,14	Cooling temperature	T_{FC}	11 h	70 °C
15,16	Cooling temperature	T_{FC}	11 h	65 °C
17	100 h measurement	-	100 h	-
18	Reverse flow	co-, counterflow	1 h	-

3.2. Preprocessing of the Current Density Measurement

Analysis of the measurements has shown that a preprocessing from 2D to 1D of the measurement data is beneficial for the understanding of the results. The measurements of the sensors are put in order according to the channel structure of the bordering anode bipolar plate to get a current density along the channels from inlet to outlet. For demonstration in Figure 4 the current density profile at the nominal operation point of 500 mA/cm^2 is shown for the outlet cooling water temperatures of 25 and 65 °C. The x-axis denotes the normalized channel structure from inlet (x = 0) to the outlet (x = 1) of the bipolar plate. This preprocessing allows analyzing the impact of parameter changes on the inlet and outlet area of the cell as well as the change during the flow through the channel geometry, e.g., humidity changes from inlet to outlet.

The channel structure of the bipolar plate is a meandering pattern. At each redirection of the gas channel a current density step is noticeable. The redirection occurs after four sensor segments and corresponds to a gridline in y-direction. The profile of the current density shows the lowest value at the channel inlet. After the current density is increased to the maximum amount at the middle of the channel, a slight decrease to the channel outlet can be seen. The influence on the current density due to changes of the operation parameters of the fuel cell are analyzed in Section 4.

Figure 4. Current density profile over the normalized channel length.

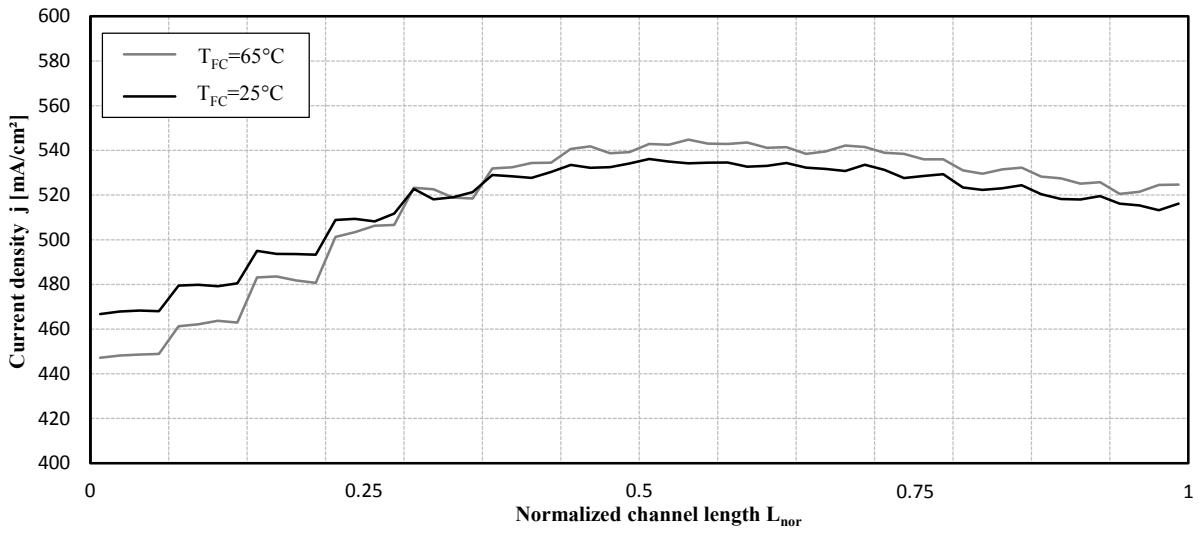

4. Results of the Current Density Measurement

4.1. Anode

4.1.1. Recirculation

The modification of the pump rotation speed inside the recirculation circle does not lead to a significant change in either the current density profile or the cell voltage in the range between 50% and 100% of the rotation speed (Figure 5a); equal to a linearized range between λ_{H2} = 1.33 and 2.0 based on the sum of the mass flow of recirculated and fresh hydrogen]. In the series of measurement 2, the maximum spread of the current density decreases with increasing rotation speed in the nominal

operating point. However, the series of measurement 3 (with an identical set of parameters as in 2) shows the opposite process of the current density; namely a slight decline of the current density at the inlet and an increase at the outlet. The maximum spread rises to 110 mA/cm^2.

The proportion of recirculated hydrogen to fresh hydrogen increases in the blending point when the pumping rotation speed increases. The result is an increase in temperature of 11 °C at the entry point. The reduction of the operating point to 250 mA/cm^2 at constant pumping rotation speed increases the entry temperature by another 4 °C to a temperature of 52 °C (Figure 5b).

Figure 5. Current density and hydrogen temperature profile *vs.* rotation speed recirculation pump. (**a**) Current density profile at 0.5 A/cm^2 for 50 (λ_{H2} = 1.33) and 100% (λ_{H2} = 2.0) rotation speed of recirculation pump and (**b**) H_2 temperature profile at gas in- and out-let for 0.25 and 0.5 A/cm^2 between 50% and 100% rotation speed of recirculation pump.

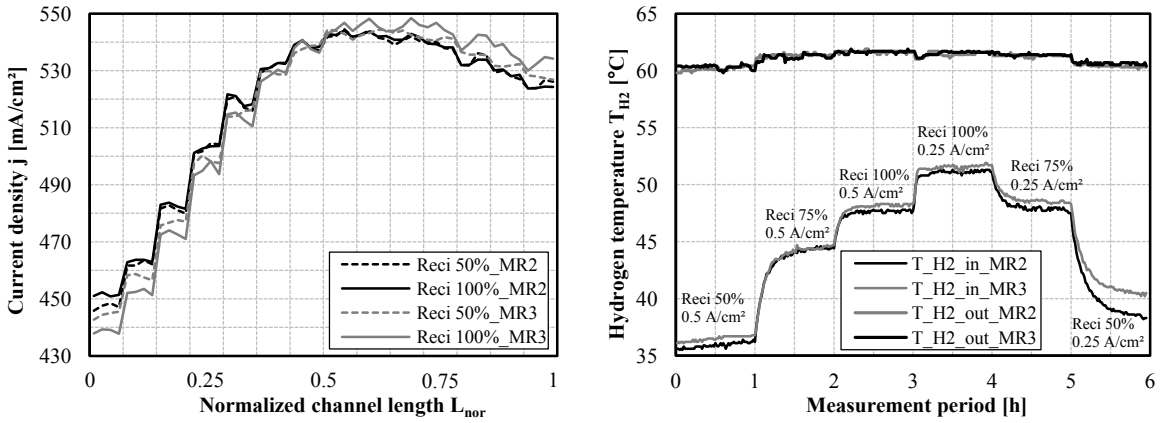

(**a**) (**b**)

In another measurement, the rotation speed of the recirculation pump was reduced down to 25% and switched off afterwards (Figure 6a). Only after the pump was switched off, the homogenous profile of the current density tilts within 4 s. At the inlet the current density rises from 450 to 580, while at the same time it falls down at the outlet from 520 to 330. Especially in the final third of the course of the channel, significant leaps appear at the deflections of the gas channels (every gridline in y-direction indicates a change of direction of the channel structure). The missing suction effect of the pump leads to a condensation of water drops in the gas panel. The steady current demand of the load is temporarily equalized up to half of the channel length by higher segment current densities. The partial undersupply of the anode leads to a steep decline of the final cell voltage.

Reducing the rotation speed from 100% to 80% at a stack temperature of 70 °C leads to a slow tilting over of the current density profile within 66 s (Figure 6b). The blockage of the gas panel with water drops in the entry area successively blocks the supply of hydrogen in the second half of the channel, which in turn leads to a steep drop of the first two cell voltages. The hydrogen circulation influences the temperature, mass and humidity relations of the anode. The effect on the current density profile, however, is very small for the tested system with four cells. The partial flooding of the anode leads to a significant shift of the maximum and minimum current density areas at the switching off and causes a change of the rotation speed.

Figure 6. Reduction rotation speed of recirculation pump and overturning of current density profile. (**a**) Overturning of current density profile after cut off of recirculation pump and (**b**) water flooding at the H_2 entrance after reducing rotation speed of recirculation pump. Starvation along the gas channels.

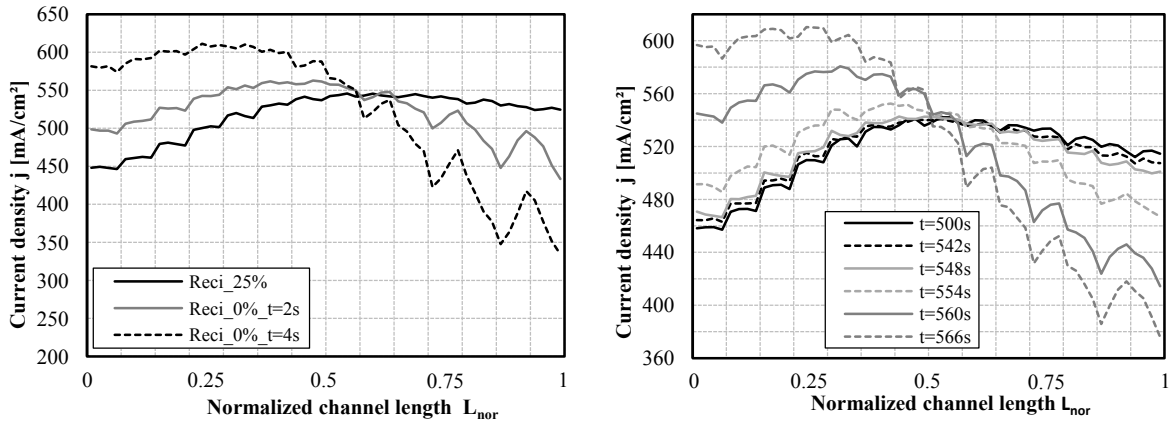

(**a**) (**b**)

4.1.2. Purge Interval

The purge interval of 90 s has been extended by 60 s steps up to a maximum of 11 min after every hour for the series of measurement 4 and 5. The current density profile neither changes directly before or after a purging nor does it change between two phases of purging. The extension of the purging interval has no effect on the cell voltage as well (Figure 7).

Figure 7. Current density profile during purging and within the purging interval. (**a**) Profile directly before/after purging and (**b**) profile within a purge interval of 11 min.

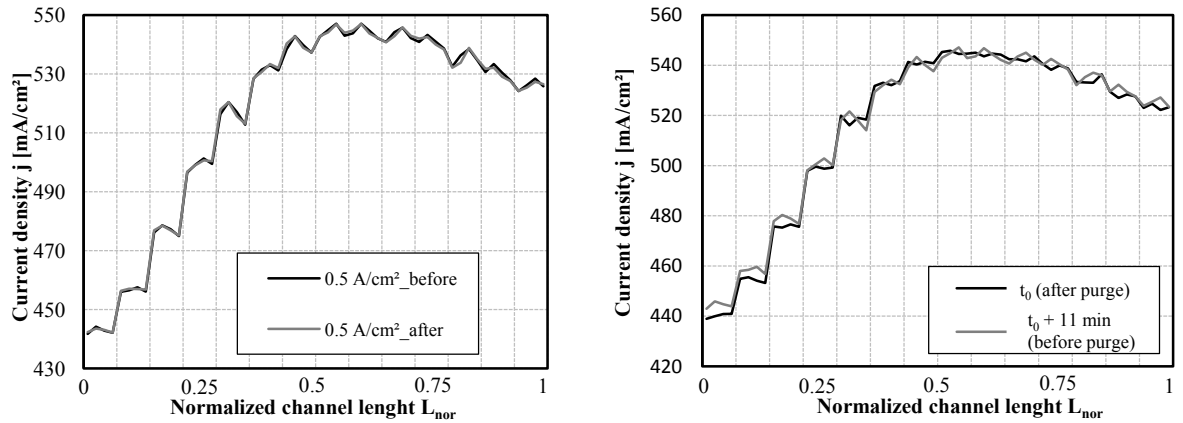

(**a**) (**b**)

This means that the recirculation, when at a sufficient rotation speed, does not allow any accumulation of water and foreign gas enrichment. Instead it creates a stable operation, due to the suction effect at the outlet, independent of the length of the intervals [12].

4.2. Cathode

4.2.1. Stoichiometry

In this study, the cathode stoichiometry is varied between 2.0 and 4.0, whereby the reference stoichiometry is 2.5. The cathode stoichiometry affects the current density profile significantly stronger than at the anode.

The stoichiometry of 2.0 leads to minimization of the maximum spread of the current density profile and a shift of the maximum values towards the inlet (Figure 8a). The spread is less than 100 mA/cm^2. The lower flow velocity of the air at the inlet leads to a significant increase of the current density. That is due to the higher diffusion time of oxygen at the transfer from the gas channel into the gas diffusion layer and due to the lower evaporation rate of the process air to absorb the product water of the fuel cell reaction. At the outlet of the cell, a strong lowering of the electricity production is recognizable, which nonetheless is still well above the current density values at the entrance. The concentration of oxygen is already decreasing more strongly along the channel, due to the lower entry level, so that a beginning mass transport limitation occurs at the final third of the channel. The latter is enforced by the lower evaporation rate of the product water. The air absorbs sufficient water steam in the gas diffusion layer (GDL) surface and gas channel area in the first third of the channel course. Supersaturated conditions do stop the absorption of product water by the air. The emerging condensation makes the transport of oxygen more difficult. After only a few min this leads to the jittering of the last cell and to a lowering of the cell voltage of cell number 4 by 8% (Figure 8b). With a lower stoichiometry one can achieve an optimum of the current density profile, but not a stable voltage for the lowest cell. The later can only be countered by a lowering of the air inlet humidity. The increase of the air stoichiometry from 2.5 to 3.0 has the opposite effect.

Figure 8. Current density profile and cell voltage for increasing air stoichiometry up to 3. (**a**) Current density profile by increasing air stoichiometry from 2 to 3 and (**b**) changing of cell voltage for different air stoichiometry related to λ_{air} = 2.5.

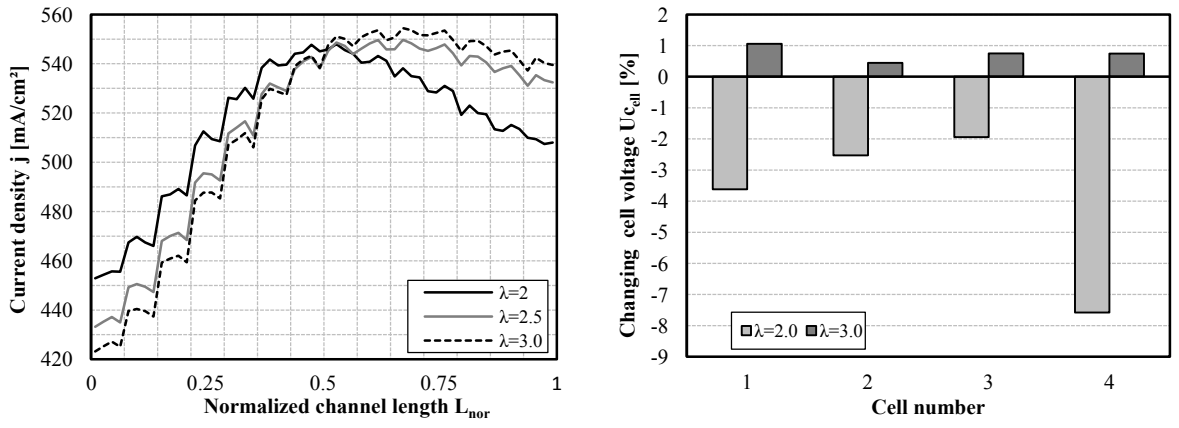

(**a**) (**b**)

The increase of the flow velocity minimizes the diffusion time and increases the convective drying out at the inlet. The profile rises at the outlet to maximum values.

The higher concentration of the air at the outlet is sufficient to keep the transport pathways clear and to achieve balanced humidity conditions in this part of the membrane surface.

A further increase of the air stoichiometry up to 3.5 and 4.0 intensifies the drying out in the inlet areas of the cells and leads to a further decline of the electricity production by 6%, respectively to a higher membrane resistance, whereby the maximums are shifting further towards cell exit (Figure 9a). Due to the increasing maximum deviations of the current density profile and a higher load at individual membrane areas, stoichiometry above 3.0 is not recommended because of the expected quick aging (dry conditions at the entrance, higher current loads at the exit). The energetic additional requirement for the supply of the process air is higher than the performance gain of the fuel cell. The cell voltages increase, related to the stoichiometry of 2.5, by 1.5% up to 4.3% (Figure 9b).

Figure 9. Current density profile and cell voltage for increasing air stoichiometry up to 4. (**a**) Current density profile by increasing air stoichiometry from 2.5 up to 4 and (**b**) increased cell voltage for different air stoichiometry related to λ_{air} = 2.5.

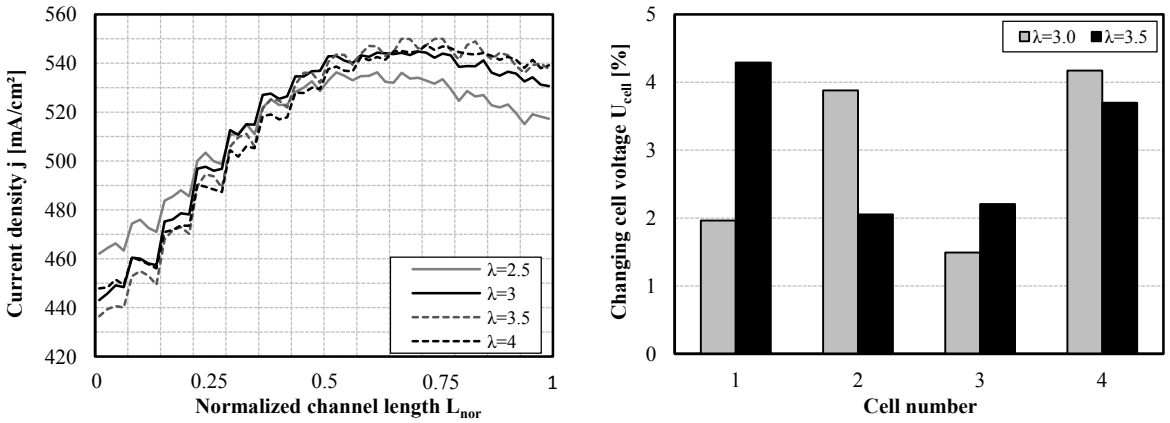

4.2.2. Air Inlet Temperature

The air inlet temperature was 63 °C for the previous examinations with a stable coolant exit temperature of 65 °C. The air stoichiometry is 3.0 and therefore higher than the previous comparative measurements, since voltage jittering occurred increasingly at the final cell. During the series of measurements 9, the air inlet temperature has been lowered from 63 down to 59 °C and after a hold time of one h it has been warmed up to a coolant exit temperature of 65 °C (Figure 10a). The lowering of the temperature leads to a slight voltage increase in all four cells. The temperature transition results in an increase of the evaporation rate of the product water, which improves the humidity conditions for the short-time measurements and raises the cell potential slightly. An additional temperature change of the air to coolant temperature minimizes the voltages of all cells, since the give off of water droplets of the product water declines. The current density profile shows a significant decrease at the inlet for an air temperature of 59 °C. The current densities increase slightly in the middle part of the channel course. In the series of measurements 17 in Figure 10b, the air inlet temperature of 59 °C was held stable for 30 h. The current density profile changes, like in the series of measurements 9, and stays there for the entire measuring period. A further decrease of the current density at the inlet does not

occur. The cell voltages fall gradually by 12 mV. So the increase of the voltage of the short-time measuring in the measuring interval of one hour lasts only shortly. In contrast to the series of measurements 9, it was possible to minimize the stoichiometry again from 3.0 to 2.5 during the long-time measuring, since the increasing give off of product water, caused by the process air, resulted in a stable tension behavior of the final cell.

Figure 10. Reduction of the air inlet temperature. (**a**) Reduction of the current density at the inlet after reducing of $T_{Air,in}$ and (**b**) long-term behavior of the current density profile for an air temperature of 59 °C and constant stack temperature of 65 °C.

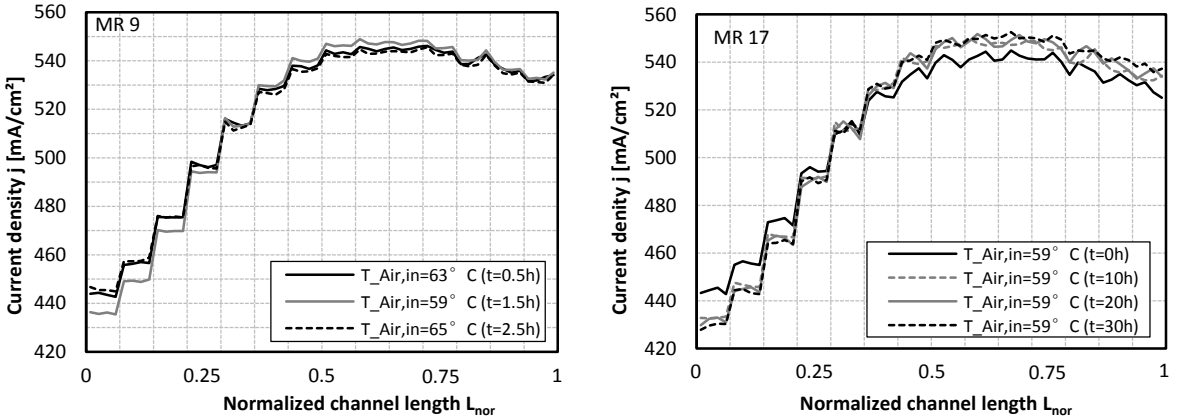

(**a**) (**b**)

4.3. Cooling

Temperature

With increasing cell temperature the reaction kinetics of the electrodes are improved. With increasing temperature of the cooling water at the outlet from 65 to 70 °C the temperatures of the reactant gases rise by 5 °C as well.

The results from increasing temperatures in Figure 11a lead to significant differences at the inlet and outlet. While the maximum spread for 65 °C is almost 120 mA/cm^2, the increase to 70 °C shows the lowest spread of all the measurements of 90 mA/cm^2. The voltage of the two middle cells rises to the level from the beginning of the measurements (Figure 11b). The voltage at cell 1 shows no reaction and stays at a constant level. The last cell drops slightly in voltage with the temperature increase.

Figure 11. Profile of the current density along the channel length for rising coolant temperatures. (**a**) Profile of the current density along the channel length for rising coolant temperatures and (**b**) voltages for varying fuel cell temperatures.

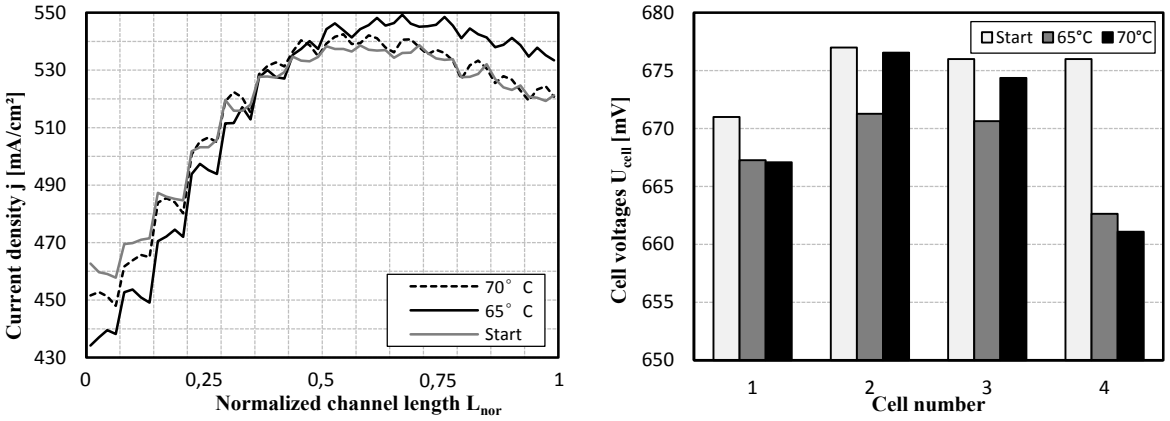

(**a**) (**b**)

4.4. Change of Flow at Anode and Cathode

Change of Flow

Our next investigation examined the question of whether the current density profile changes if the direction of the gas flow is changed (anode inlet becomes anode outlet, *i.e.*, air). For this purpose three short-time measurements were performed using another test system. In the first measurement the hydrogen was fed in the original anode outlet of the fuel cell while the flow direction at the cathode was not changed. In the second measurement the flow direction at the cathode was changed and in the third measurement both gases (*i.e.*, at anode and cathode) were fed to the cell vice versa. For every measurement the current density-voltage-characteristics (0.1–0.5 A/cm^2) were recorded with a hold time of two min per measuring point. The current density profile is compared to the prior series of measurement 17.

In Figure 12a, the current density profiles of the measurement *anode* are shown for five operation points in comparison to the current density profile of the prior measurement (dashed line). The profile clearly rises in the nominal operating point at the hydrogen inlet. At the outlet the current density falls in comparison to the reference measurement.

The inversion of the flow direction at the cathode results in an increase of the current density at the inlet (Figure 12b, inlet right side) and a stronger decrease at the outlet in comparison with the reference measurement. Compared to the other measurements, the maximum deviations of the current density are higher for all measuring points. The concentration at the cathode influences the profile stronger than at the anode.

As soon as both media flow in the same direction through the cells, no differences to the reference measurements (at least for the short-time measurement) are recognizable (Figure 12c). Further examination is required if a constant change of the flow direction of both gases, e.g. after every restart, minimizes the areas of strong degradation at the gas inlet, as identified according to Pei *et al.* [13], and contributes decisively to the increase of lifetime.

The current density profile can be influenced only slightly by the change of the flow direction within the examined parameter areas. The segments of high current generation remain in the second half of the channel, so that there is no relief and distribution to other segments. The voltages of the four cells (cell 1 on the top, outlet) are the highest for change of flow direction at the cathode and for change on both sides (Figure 12d). As reference the voltages at the beginning of measurement series 17 (normal start) and after 100 h measuring time are taken.

Figure 12. Change of flow direction at anode and cathode. (**a**) Current density without (dashed) and after change of flow direction at anode; (**b**) current density without (dashed) and after change of flow direction at cathode; (**c**) current density without (dashed) and after change of flow direction at anode and cathode (not dashed); and (**d**) comparison of the cell voltage behavior after change of flow direction, during normal operation at the beginning of measurement and after 100 h for 500 mA/cm^2.

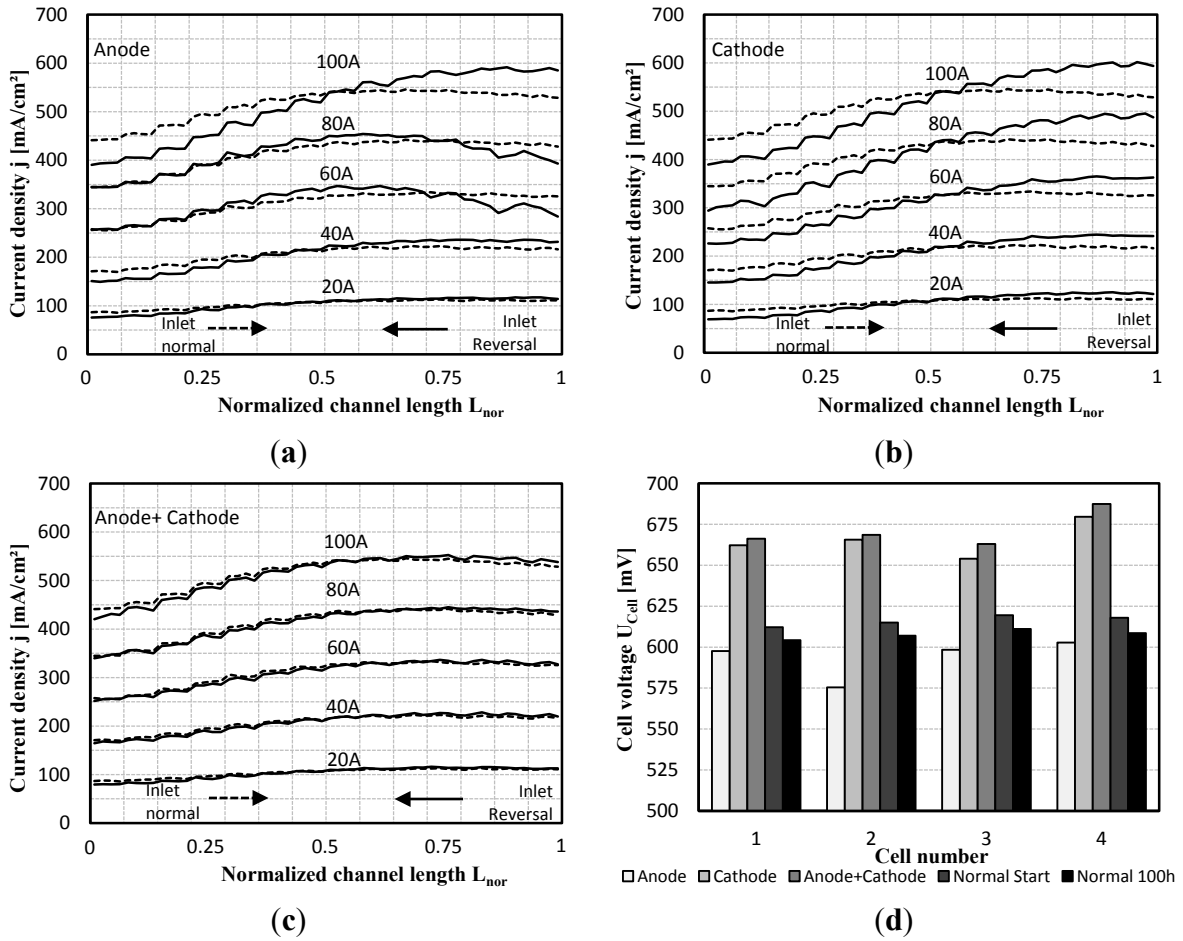

4.5. Long-Term Analysis

The long-term behavior of the average cell voltages of the four cells as well as the corresponding segment current density at the inlet and outlet at the nominal operation point of 500 mA/cm^2 in Figure 13 (respectively in 1 h intervals) show no significant shifts to higher or lower values for the segment current densities for the majority of the measurements. In general, the long-term measurements lead to an increased spreading of the current density. In short-term operation the segment current densities are

closer to each other. At the section of the 117th h a strong decrease of the cell voltages and the current density at the inlet can be noticed. The reason is the faulty volume flow rate for the air supply. Dehydration at the inlet reduces the current density production, which is compensated through the segments at the outlet. While the level of the cell voltages in short-term operation and the first long-term operation stays above 650 mV (20–288th h), the dry conditions of the second long-term measurement (289–383th h) result in a strong cell voltage decrease. In the final measurement, with reversed direction of flow and better humidity balance, the voltage level of the first measurement was nearly reached. The system shows in total a degradation of 19.5 μV/h. A current density production decrease of 137 μA/h at the inlet and an increase of 132 μA/h at the outlet are the result of the operation. These degradation values (Table 4) cannot be taken directly from Figure 13. The cell voltages presented are measured at different parameters and are not comparable. The values are clearly below the degradation values in comparison to each individual measurement, which are caused by the parameter variation and led to the fluctuations between h 88 and 383 in Figure 13. The discontinuous operation of the system led eventually back to the original cell voltages [14] and segment current densities.

Figure 13. Long time behavior of cell voltage and current density.

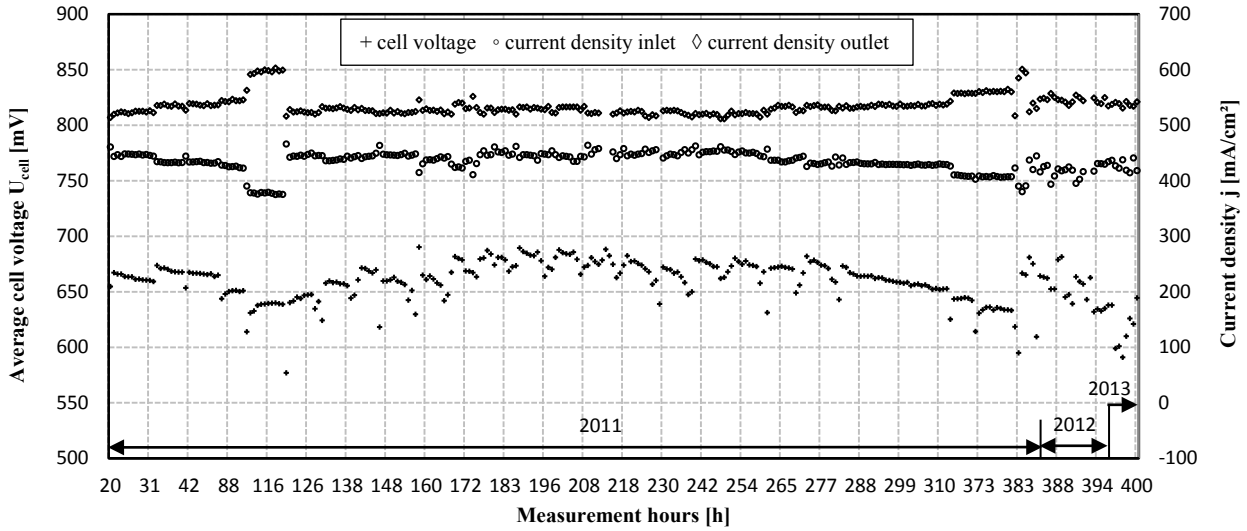

Table 4. Degradation of the fuel cell stack after 20 and 400 operation h; measurement each after constant phase with identical parameters (see Figure 3).

Operation (h)	Average cell voltage (mV)	Current density inlet (mA)	Current density outlet (mA)
$t = 20$	651.5	465.9	500.5
$t = 400$	644.1	413.9	550.6
Degradation	−19.5 μV/h	−137 μA/h	+132 μA/h

A vectorial experiment scheme was created to analyze the effects of single and combined (cross effects) changes of the operation parameters on the current density profile (CDP) and single cell voltages (SCV). The parameters include stack temperature, cathode stoichiometry and air inlet temperature. The upper and lower values are given in Table 5 and are marked with "+" and "−" in the results while the parameters are symbolized by "A", "B" and "C" for simplification. Because

recirculation pump speed and purge interval did not show a significant impact, these parameters were not changed during this test.

$$n = n_s^{\,n_f} \tag{2}$$

with n_s = Number of values tested (+ and −), n_f = Number of analyzed parameters.

Table 5. List of analyzed parameters.

Parameter	Symbol	Value "–"	Value "+"	Unit
Stack temperature T_{FC}	A	55	65	(°C)
Cathode stoichiometry	B	2.9	3.3	(-)
Air inlet temperature	C	T_{FC}-2 °C	T_{FC}-4 °C	(°C)
Recirculation pump speed	-	60	60	(%)
Purge interval	-	30	30	(s)

Equation (2) results in 8 required measurements for the vectorial experiment scheme with the three analyzed parameters [15]. The complete experiment scheme is given in Table 6. The cross effects of combining AB, BC and AC and all three together in ABC were added to the scheme.

Table 6. Vectorial experiment scheme.

Number	A	B	C	AB	BC	AC	ABC
1	-	-	-	+	+	+	-
2	+	-	-	-	+	-	+
3	-	+	-	-	-	+	+
4	+	+	-	+	-	-	-
5	-	-	+	+	-	-	+
6	+	-	+	-	-	+	-
7	-	+	+	-	+	-	-
8	+	+	+	+	+	+	+

To determine the effects E of the parameters y and the cross effects, Equation (3) is used to subtract the averaged measurement values of the parameters according to the setting [16].

$$E_A = \frac{y_2 + y_4 + y_6 + y_8}{4} - \frac{y_1 + y_3 + y_5 + y_7}{4} \tag{3}$$

In Figure 14, the calculated effects for the SCV and CDP measurements are given. The levels represent the impact of the change of parameters (or their combination) on the target value (SCV or CDP).

The SCV is only dependent on the main parameters A, B and C while cross effects have almost no impact on the target value. The stack temperature (A) has the biggest impact, the cathode stoichiometry (B) and air inlet temperature (C) are have nearly the same (lower than A) impact. But the cross effects have to be taken into account as well. While the combined change of A and B has almost no effect, the other cross effects are very small. That means setting all parameters to value "+" is not the best option.

For the CDP the diagram shows a different behavior. The parameter B has the only noteworthy impact on the CDP. Combining B with A or A and B results in almost no effect on the CDP, only the combination of B and C or A and C shows a slight impact

Figure 14. Diagram of the impact effects on SCV and CDP.

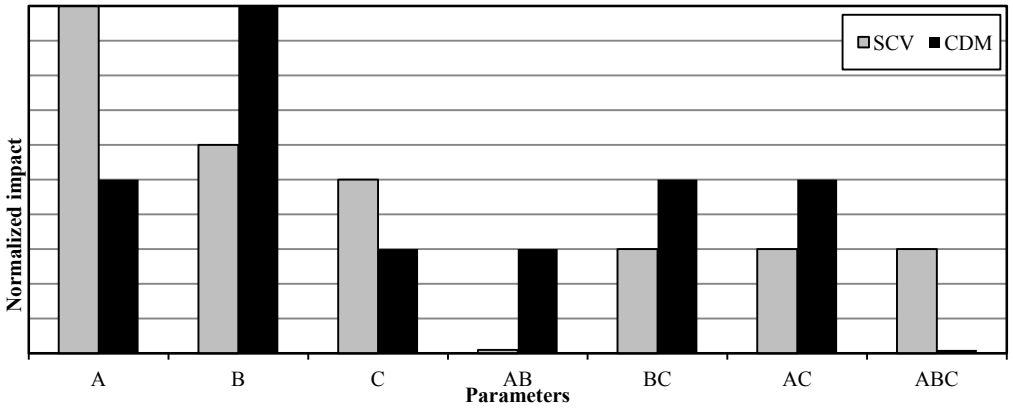

5. Conclusions

The CDM developed in [10] was field-tested over the past two years. The testing involved over 70 starts and stops with long offline periods in order to analyze the behavior and optimize the critical operation points. During operation the stoichiometry of the cathode had the most influence on the current density profile due to the large impact on the humidity balance of the PEMFC. When the current density profile is widely spread the cell voltages are lower or unstable. The current density profile is lowest at the channel entrance, it increases to the middle of the channel where it reaches its maximum and then decreases towards the end of the channel. This profile appears to be a permanent characteristic for the cell as it cannot be changed significantly by reversing the flow direction of the reactants. Long-term analysis shows an increase of the spreading of the current density profile up to 130–140 mA/cm^2 at the nominal operation point of 100 A. This could either be the result of running-in of the cells or it could be a first evidence for aging. The cell voltages return to the original values after some operation time and show no signs of aging, however, the system seems to be stable over the long-term. This proofs the significance of the CDM compared to the cell voltage measurement, as the CDM reacts faster and gives information about changes which cannot be monitored by the cell voltages. Such being the case, the current density spread analysis could be a new method to verify aging earlier and independent of cell voltage measurement, as well as react faster to change the operating conditions in a way to reduce the aging. To confirm this method more comparison measurements are planned. The placement of the CDM has to be tested at the first and last cells as well as in the middle of stacks with many more cells to show the impact of core temperature, especially in combination with the humidity balance. Control strategies to improve the lifetime and power output according to the found dependencies of the CDM and the operation conditions need to be developed and long-term tested to verify an impact on the aging of fuel cells, which cannot be achieved solely through the common cell voltage measurement.

Conflict of Interest

The authors declare no conflict of interest.

References

1. Weber, A.Z.; Newman, J. Modeling transport in polymer-electrolyte fuel cells. *Chem. Rev.* **2004**, *104*, 4679–4726.
2. Jiao, K.; Li, X. Water transport in polymer electrolyte membrane fuel cells. *Prog. Energy Combust. Sci.* **2011**, *37*, 221–291.
3. Wang, C.-Y. Fundamental models for fuel cell engineering. *Chem. Rev.* **2004**, *104*, 4727–4765.
4. Hottinen, T.; Himanen, O.; Lund, P. Performance of planar free-breathing PEMFC at temperatures below freezing. *J. Power Sources* **2006**, *154*, 86–94.
5. Lobato, J.; Cañizares, P.; Rodrigo, M.A.; Pinar, F.J.; Úbeda, D. Study of flow channel geometry using current distribution measurement in a high temperature polymer electrolyte membrane fuel cell. *J. Power Sources* **2011**, *196*, 4209–4217.
6. Yuan, X.; Wang, H.; Colin Sun, J.; Zhang, J. AC impedance technique in PEM fuel cell diagnosis—A review. *Int. J. Hydrog. Energy* **2007**, *32*, 4365–4380.
7. Gerteisen, D.; Mérida, W.; Kurz, T.; Lupotto, P.; Schwager, M.; Hebling, C. Spatially resolved voltage, current and electrochemical impedance spectroscopy measurements. *Fuel Cells* **2011**, *11*, 339–349.
8. Markötter, H.; Manke, I.; Krüger, P.; Arlt, T.; Haussmann, J.; Klages, M.; Riesemeier, H.; Hartnig, C.; Scholta, J.; Banhart, J. Investigation of 3D water transport paths in gas diffusion layers by combined in-situ synchrotron X-ray radiography and tomography. *Electrochem. Commun.* **2011**, *13*, 1001–1004.
9. Klages, M.; Enz, S.; Markötter, H.; Manke, I.; Kardjilov, N.; Scholta, J. Investigations on dynamic water transport characteristics in flow field channels using neutron imaging techniques. *J. Power Sources* **2013**, *239*, 596–603.
10. Geske, M.; Heuer, M.; Heideck, G.; Styczynski, Z.A. Current density distribution mapping in PEM fuel cells as an instrument for operational measurements. *Energies* **2010**, *3*, 770–783.
11. Heideck, G. Ein Autonomes Brennstoffzellensystem–Optimierungsansätze [in German]. Ph.D. Thesis, Otto-von-Guericke-Universität Magdeburg, Magdeburg, Germany, 2006, ISBN 3-929757-94-X.
12. Bernstein, P.; Heuer, M.; Heideck, G.; Styczynski, Z.A. Impact Study of Hydrogen Utilization in PEM Fuel Cell Systems. In Proceedings of the 4th World Hydrogen Technology Convention (WHTC2011), Glasgow, UK, 14–16 September 2011.
13. Pei, P.; Yuan, X.; Chao, P.; Wang, X. Analysis on the PEM fuel cells after accelerated life experiment. *Int. J. Hydrog. Energy* **2010**, *35*, 3147–3151.
14. Schätzle, M.; Scholta, J.; Pawlik, J.; Jörissen, L. Influence of Start-Stop-Procedures on PEMFC Degradation. In Proceedings of the International Workshop on the Effects of Fuel & Air Quality to the Performance of Fuel Cells, Berlin, Germany, 9–11 September 2009.
15. Siebertz, K. *Statistische Versuchsplanung: Design of Experiments (DoE)*; Springer-Verlag: Berlin, Germany, 2010.

16. Ryan, T.P. *Modern Experimental Design*; John Wiley and Sons: Hoboken, NJ, USA, 2007.